Journal of Materials Chemistry C

ROYAL SOCIETY OF CHEMISTRY

PAPER

View Article Online
View Journal

Cite this: DOI: 10.1039/d6tc01050d

Ultra-long WSe_2 nanotubes and related hybrid nanostructures

Vojtech Kundrat, *[abc] Vaclav Huzlik, [a] Stepan Kusak, [a] Ramon Pina Brito, [d] Dido Denier Van der Gon, [d] Stuart Robertson, [e] Zhaoxia Zhou, [e] Kristyna Bukvisova, [c] Lothar Houben, [f] Xiaoyu Guo, [g] Yao Guo, [g] Paola Ayala [d] and Reshef Tenne *[b]

Received 1st April 2026,
Accepted 26th May 2026

DOI: 10.1039/d6tc01050d

rsc.li/materials-c

Ultra-long WSe_2 nanotubes were synthesized *via* continuous selenidation of ultra-long $W_{18}O_{49}$ nanowhiskers. A modified reactor configuration enabling a sustained selenium vapor supply allowed complete conversion of the oxide nanowhiskers into hollow WSe_2 nanotubes with lengths reaching hundreds of micrometers, while keeping diameters below 100 nm. Detailed structural characterization confirmed the multilayered 2H-WSe_2 structure and hollow morphology. Controlling the reaction time enables the synthesis of both hybrid $W_{18}O_{49}$@WSe_2 core–shell nanowhiskers and 1D/2D nanotube–plate hybrid structures. Optical characterization revealed excitonic emission and polariton-related optical features arising from light confinement within the nanotube cavity. Electrical measurements on single-nanotube devices demonstrated semiconducting behavior with nonlinear *I–V* characteristics and a clear photoresponse under laser illumination. Together, these ultra-long WSe_2 nanotubes and hybrid structures offer a versatile platform for optoelectronic, photonic, and catalytic applications.

Introduction

Transition metal dichalcogenides (TMDs)[1] and metal oxides are of significant interest in materials science due to their unique structural, optical, and electrical properties. TMDs, such as WS_2, WSe_2, and MoS_2, exhibit a strong number of layer-dependent electronic and optical effects, making them ideal candidates for applications in nanoelectronics, optoelectronics, and catalysis.[2,3] On the other hand, metal oxides[4] play a crucial role in various technological applications, including sensing, catalysis, and energy storage.[5,6] Combining these materials into hybrid nanostructures not only opens the possibility to gain control over the material's functionality, but it also provides access to improved mechanical properties and controlled reactivity, particularly in harsh environments. Furthermore, the formation of heterogeneous structures allows the optoelectronic properties of the individual components to be tuned, with a potential for new applications.

One well-integrated member of the 1D/2D materials family stands out thanks to its tunable properties, *i.e.* inorganic nanotubes (NTs).[7,8] The electronic structure of the NTs is dominated by the inherent strain in the structure, which overcomes the effect of quantum size confinement.[9–11] For small-diameter nanotubes, this results in highly modified optoelectronic properties, a small band gap, or even a transition from semiconducting to metallic behavior for small-diameter tubes.[12,13] WS_2 nanotubes with large diameter (>80 nm), on the other hand, demonstrate a strong light–matter interaction.[9,10] These NTs support optical cavity modes owing to their large refractive index (>4) in the visible range. Photon confinement within the cavity drives quantum mechanical coupling between the cavity mode and excitons, giving rise to hybrid half-light, half-matter moieties known as polariton modes with a Rabi gap >150 meV.[10,14] Harnessing this light confinement effect in semiconducting TMD nanotubes holds significant promise for quantum information technologies and next-generation memory devices.[15–17] Recently, submillimeter WS_2 nanotubes materialized thanks to the high-temperature sulfidation of ultra-long tungsten suboxide nanowhiskers (aspect ratio reaching 2000–5000).[18] First, ultra-long W_5O_{14} nanowhiskers were prepared by heating WO_3 nanoparticles in a closed ampule.

[a] Department of Chemistry, Faculty of Science, Masaryk University, Kamenice 5, Brno 62500, Czechia. E-mail: vojtechkundrat@mail.muni.cz
[b] Department of Molecular Chemistry and Materials Science, Weizmann Institute of Science, Herzl 234 St, Rehovot 7610001, Israel. E-mail: reshef.tenne@weizmann.ac.il
[c] Thermo Fisher Scientific, Vlastimila Pecha 12, 62700 Brno, Czech Republic
[d] University of Vienna, Faculty of Physics, Strudlhofgasse 4, 1090 Vienna, Austria
[e] Department of Materials, Loughborough University, Epinal Way, Leicestershire, LE11 3TU, UK
[f] Department of Chemical Research Support, Weizmann Institute of Science, Herzl 234 St, Rehovot 7610001, Israel
[g] Centre for Quantum Physics, Key Laboratory of Advanced Optoelectronic Quantum Architecture and Measurement, School of Physics, Beijing Institute of Technology, Beijing, 100081, China

High-temperature sulfidation of the ultra-long tungsten suboxide nanowhiskers was facilitated by gaseous H_2S, which could be supplied to the reaction over an extended reaction time. These WS_2 nanotubes were applied for the preparation of a paper-like material, which was further exploited in the ultrafiltration of gold nanoparticles. Building on these advances, a network of long, slender WS_2 NTs[19] was recently employed to realize an optogenetic-like neuromorphic computer capable of distinguishing between malignant and healthy tissues. Although WSe_2 NTs have been described in the literature by a number of authors, they have remained limited to relatively short (a few μm) 1D nanostructures.[14,20–22]

Extending the length of WSe_2 nanotubes to macroscopic dimensions would substantially broaden and naturally enhance their application potential, particularly in the field of optoelectronic devices, leveraging their 1D nanoscopic character and strain-engineered properties, while offering the practical advantages of macroscopic handleability. However, scaling up these structures poses significant synthetic challenges, primarily due to the limited availability of continuous selenidation precursors and the inherent constraints of elemental selenium as a selenidation agent, necessitating a departure from conventional gas-phase sulfidation processes. The synthetic protocol developed in this work directly addresses these challenges. Our experimental findings follow.

Results and discussion

In the previous study,[18] WS_2 nanotubes up to 300 μm long and an aspect ratio of up to 5000 were reported. For this synthesis, very long W_5O_{14} nanowhiskers were prepared first by a closed ampule reaction. For that purpose, hydrogen tungsten bronze was heated at high temperatures in a sealed quartz ampule. The nanowhiskers were subsequently sulfidated in a flow reactor using H_2S and forming gas (N_2 : H_2 gas mixture in a 95 : 5 ratio) as precursors. In the present work, the protocol for synthesizing ultra-long tungsten suboxide nanowhiskers was modified to achieve even longer nanostructures of a controlled tungsten suboxide $W_{18}O_{49}$ phase (Fig. 1). Building on the synthesis of ultra-long WS_2 nanotubes,[18] the present work introduces a fundamentally modified protocol that pushes nanostructure dimensions even further and extends compositional control to the selenide family. While the previous approach relied on sulfidation of W_5O_{14} nanowhiskers, which were prepared *via* closed ampule reaction from hydrogen tungsten bronze and subsequently converted using H_2S and forming gas (N_2 : H_2 gas mixture in a 95 : 5 ratio) in a flow reactor. The strategy developed here targets a controlled $W_{18}O_{49}$ tungsten suboxide phase, yielding ultra-long nanowhiskers with well-defined composition (Fig. 1). Scanning electron microscopy (SEM), showed that extended reaction time (up to 3 h) and higher reaction temperature (900 °C) enabled forming substantially longer - up to 1 mm long $W_{18}O_{49}$ nanowhiskers (Fig. 1a and b). Comparably, when the same reaction is performed at 800 °C for 30 minutes,[18] the phase was identified as W_5O_{14} and the length was noticeably shorter (300 μm). The phase character of the prepared samples was directly confirmed by analysis of the nanowhisker cross-section using high-resolution scanning transmission electron microscopy (HR-STEM) - high angle annular dark field (HAADF) (inset Fig. 1b). The synthesized ultra-long $W_{18}O_{49}$ nanowhiskers were further processed.

The limitation of the selenidation primarily lies in the relatively short reaction time in the flow reactor, due to the batch character of the selenium input. Usually, selenium vapor is introduced into the reaction hot zone upstream by the flow of forming gas. Therefore, once evaporated, the selenium flux decreases over time, and the selenidation process diminishes gradually, giving rise to other reaction pathways. Continuous selenidation for an extended reaction time was necessary to convert the oxide core and obtain hollow WSe_2 nanotubes. For that to be accomplished, the selenium source was made of a

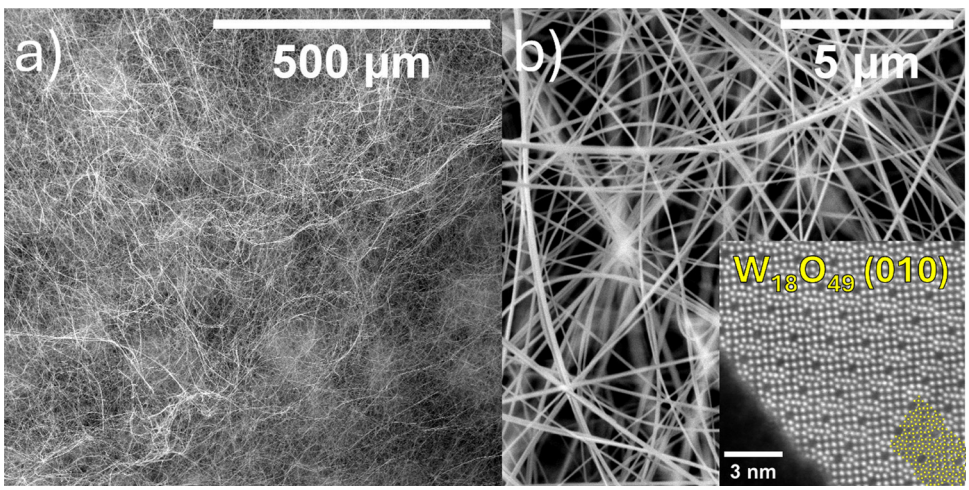

Fig. 1 (a) SEM analysis of the prepared $W_{18}O_{49}$ ultra-long nanowhiskers. (b) Magnified SEM analysis of the prepared nanowhiskers with the HRSTEM-HAADF analysis of the nanowhisker cross-section, showing the lattice of $W_{18}O_{49}$ from the ⟨010⟩ direction. The yellow polyhedron model in the bottom right corner is overlaid on the lattice of $W_{18}O_{49}$.

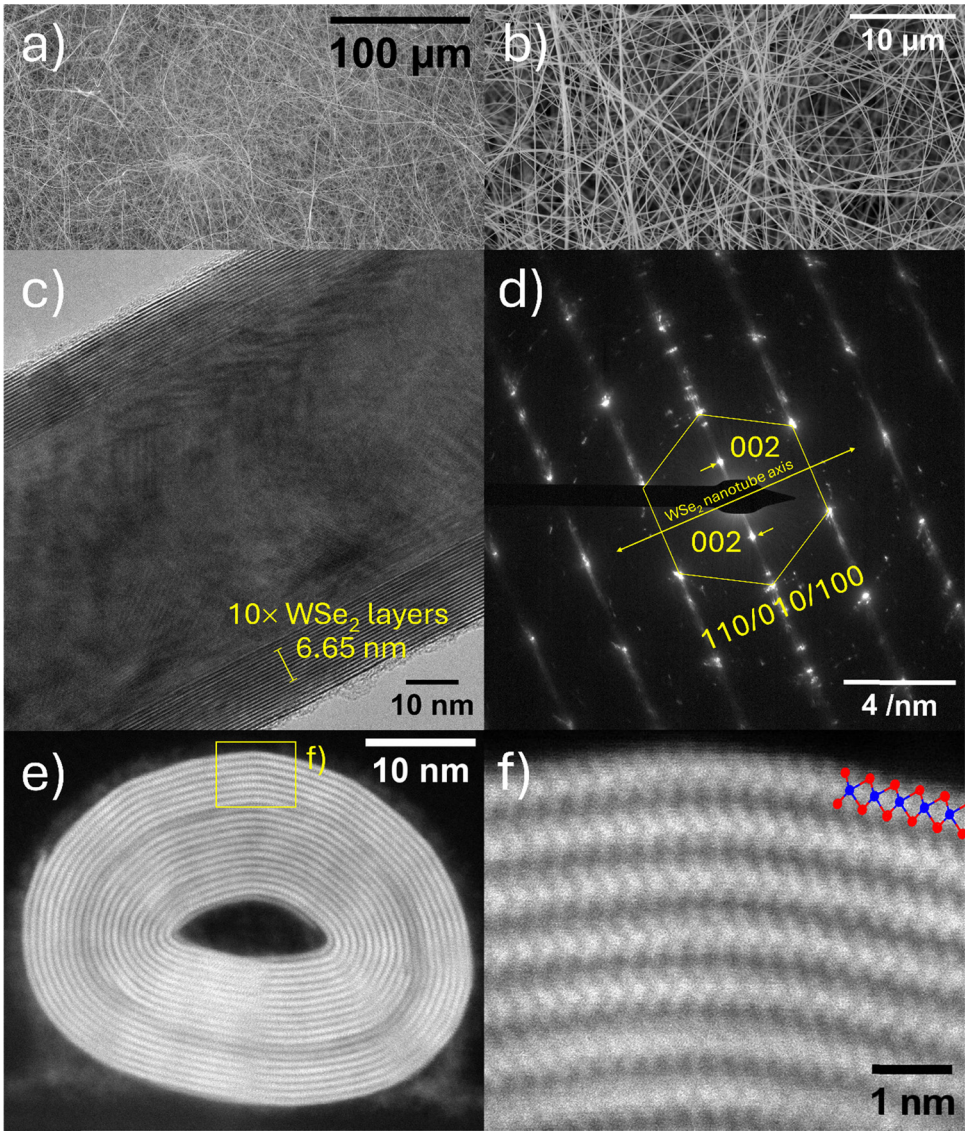

Fig. 2 Electron microscopy analyses of the ultra-long WSe_2 nanotubes. (a) and (b) SEM images of the WSe_2 nanotubes at two magnifications. (c) TEM analysis of an individual WSe_2 nanotube with indicated thickness of 10 WSe_2 layers (6.65 nm), corresponding to interlayer spacing of 6.65 Å. (d) Selected area electron diffraction (SAED) analysis of the nanotube in (c) showing a hexagonal pattern of the 2H-WSe_2 phase. Yellow arrows mark the (002) diffractions and the growth axis of the nanotube (yellow double arrow). (e) STEM-HAADF analysis of a cross-section of WSe_2 nanotube showing its oval shape and hollow core. (f) Magnified portion of the cross-section marked by a yellow rectangle in (e), revealing a 2H-WSe_2 layered lattice.

series of filled quartz crucibles positioned in line upstream of the tungsten suboxide precursor (see Fig. S1 for a schematic rendering of the reaction modulus). During the reaction, the quartz crucibles were gradually moved into the reactor's hot zone to avail the evaporation of a fresh batch of selenium into the reaction upstream. Such a strategy enabled a relatively continuous supply of selenium vapors mixed with hydrogen gas. This procedure facilitated the full conversion of the oxide nanowhiskers into tungsten-oxide-core-free (hollow) tungsten diselenide nanotubes. Fig. 2a and b display a web of (almost pure) WSe_2 nanotubes, a few hundred µm long each and <100 nm in diameter, at two magnifications. Fig. 2c shows TEM analysis of the WSe_2 nanotube with a relatively spacious lumen and approximately 20-layered walls. The lengths of the tungsten oxide nanowhiskers and the resulting WSe_2 nanotubes were estimated from SEM images (Fig. 1a and b, and the low-magnification SEM images Fig. S1b and S2a, b). Indeed, some of the nanowhiskers and nanotubes exceeded the estimated several hundreds of microns in length. However, since both 1D phases are bent and highly entangled, the exact and precise determination of the nanostructure's length is challenging. Thickness measurement of 10 layers provided an average interlayer distance of 6.65 Å, consistent with the literature.[22] The selected area diffraction (SAED) in Fig. 2d of the same WSe_2 nanotube (Fig. 2c) reveals a typical hexagonal pattern of 2H lattice in armchair arrangement,[23] marked by a yellow hexagon. The interlayer spacing (002) is marked by yellow arrows. The growth axis of the nanotube is depicted by a yellow double

arrow. The cross-section of a different WSe_2 nanotube was lifted out and measured by HRSTEM-HAADF (Fig. 2e and f). Here, the nanotubular morphology and hollow core are confirmed as well, together with the 2H arrangement in the magnified HAADF image Fig. 2f. The nanotube cross-section was found to be oval rather than perfectly cylindrical in this case, consistent with the reaction mechanism described in detail in recent publications.[24,25] The final shape and morphology of the nanotube are predominantly determined by the profile and phase composition of the precursor tungsten oxide nanowhisker. Expectably, if the shape of the precursor is irregular, the final nanotube will be non-cylindrical as well.

If the selenidation reaction is terminated before the entire oxide core is consumed, hybrid $W_{18}O_{49}$@WSe_2 core–shell nanowhiskers of sub-mm length are obtained (Fig. 3). The number of WSe_2 layers of the shell can be controlled by varying the reaction time, although complete control is not possible, likely due to the thermal mass of the oven. Fig. 3a presents HRSTEM–HAADF images of core–shell nanowhiskers with a different number of WSe_2 layers sheathing the oxide core in Fig. 3a. Fig. 3b provides a more detailed view of a single WSe_2 layer sheathing the $W_{18}O_{49}$ nanowhisker core. Additional HRSTEM-energy-dispersive X-ray spectroscopy (EDS) analysis confirmed the elemental composition, as shown in Fig. 3d and e and in the SI (Fig. S2 and S3). A lamella was prepared from a three-layer-thick core–shell nanowhisker using a focused ion beam (FIB) and standard lift-out procedure. Fig. 3c shows the STEM–HAADF analysis of such a lamella with the $W_{18}O_{49}$ core sheathed by three closed layers of WSe_2. In the magnified bottom panel of Fig. 3c, the interface between the tungsten oxide core (represented by an overlapping yellow polyhedron lattice model) and the WSe_2 layers (represented by a blue and red atom model of 2H-WSe_2) is shown in greater detail. Interestingly, the exact WSe_2–$W_{18}O_{49}$ interface is formed by a diminishing oxide phase and a nascent WSe_2 layer (marked by a yellow arrow) that appears less crystalline and ordered than the other three outer WSe_2 layers. Formation of this interfacial WSe_2 layer is in full agreement with the ''surface-inwards'' reaction mechanism observed previously.[25–27] Additionally, other morphologies have been synthesized by modifying the reaction protocol (Fig. S4a). Here, a hybrid 1D/2D WSe_2 nanotube/platelet structure is displayed (Fig. S4b–d). The EDS analysis in Fig. S4d shows a homogeneous chemical composition of both the nanotubes and the appended platelets in accordance with the WSe_2 phase. Such morphology could be obtained when the tungsten oxide nanowhisker precursor is spread out in the hot zone in a longer continuous film. There,

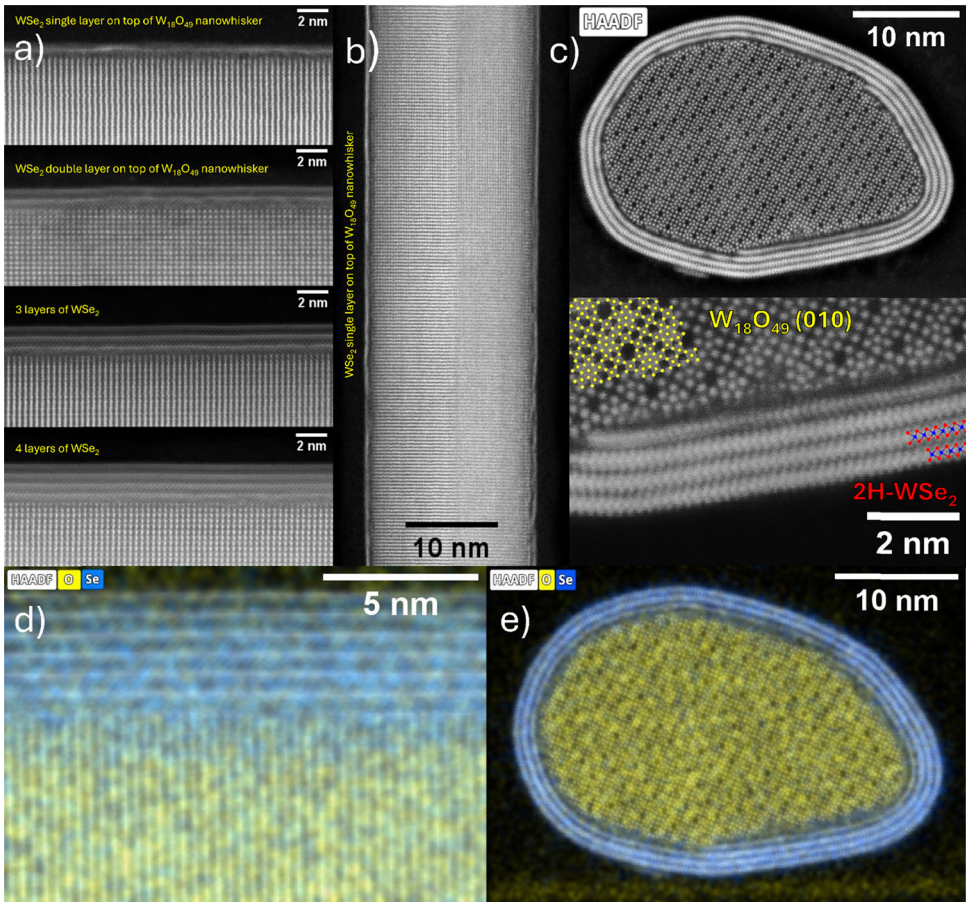

Fig. 3 HRSTEM-HAADF analysis of various core–shell $W_{18}O_{49}$@WSe_2 nanowhiskers. (a) Selected nanowhiskers with one to four WSe_2 layers sheathing the tungsten oxide core. (b) Imaging of the tungsten oxide nanowhisker with a single-layer WSe_2 shell. (c) HRSTEM-HAADF analysis of a cross-section of a $W_{18}O_{49}$@WSe_2 nanowhisker. (d) STEM-EDS mapping of a portion of the core–shell $W_{18}O_{49}$@WSe_2 nanowhisker. (e) Cross-section from Fig. 3c.

the tungsten oxide serves both as a template for the nanotube as well as a source of tungsten oxide vapors. Since the nanotube synthesis involves vapor-phase processes,[25] the evaporated tungsten oxide could react with the selenium vapor, leading to flakes deposited on the WSe_2 nanotubular backbone on the specimen further downstream (graphically depicted in Fig. S4a). Similar WS_2-based hybrid 1D/2D nanotube/plate structures have been reported previously.[28]

Ultra-long WSe_2 nanotubes can exhibit interesting (opto)electronic properties.[29,30] Fig. 4a presents the resonant Raman spectrum of a single WSe_2 multiwalled nanotube measured with a 633 nm laser wavelength. Raman modes around 251.7 and 258 cm^{-1} are assigned to normally degenerate E_{2g} and A_{1g} modes of WSe_2, respectively, although in this work, a splitting of the modes is clearly visible. It was shown before that uniaxial strain leads to lifting of the *P*63/*mmc* symmetry and the degeneracy of these two modes.[31] The Raman peak at around 303 cm^{-1} is correlated with interlayer interaction, and consequently, is not present in monolayers due to a lack of *c*-axis mirror symmetry,[32,33] as well as in bulk WSe_2, but only appears in few-layer systems. The Raman features at ~138, ~155, and ~221 cm^{-1}, together with the broad features observed between 325 and 400 cm^{-1}, are assigned to second-order scattering processes involving multi-phonon and non-Γ phonons, enhanced under resonant conditions.[33–35] In the multiwall nanotube geometry, curvature and confinement-induced symmetry reduction relax the Raman selection rules, thereby enabling the activation and enhancement of otherwise weak or symmetry-forbidden zone-edge phonons. In particular, the 221 and 240 cm^{-1} peaks are similar to the 225 and 242 cm^{-1} modes, which were attributed to disorder-induced optical modes from the K and M points in the Brillouin zone.[35] To properly understand their origin, a more detailed phonon dynamics analysis would be required, which is outside the scope of this paper. Nevertheless, compared to previously reported WSe_2 nanotubes,[14] a systematic upshift of ~5 cm^{-1} in the in-plane and second-order modes is observed, which could indicate that the Raman modes are thickness-sensitive and therefore warrant a more detailed, broader investigation.

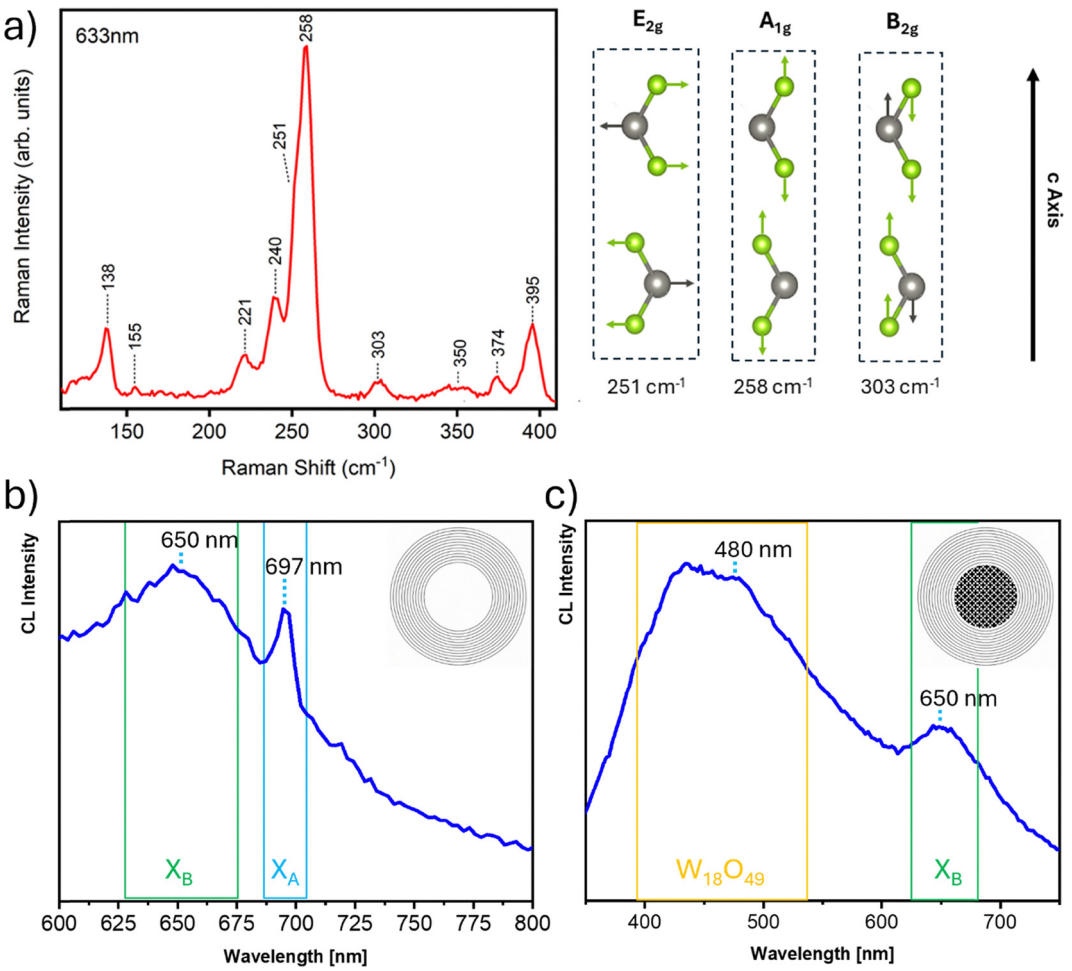

Fig. 4 (a) Raman spectroscopy analysis of the WSe_2 nanotube with the different modes shown schematically on the right. (b) Low temperature (123 K) SEM-CL spectrum of hollow WSe_2 nanotube with marked A and B exciton signals in light blue and green rectangles, respectively. (c) SEM-CL spectrum (123 K) of the $W_{18}O_{49}$@WSe_2 nanowhisker with marked WSe_2 B exciton in green rectangle and emission of the oxide core marked by the yellow one. Pictograms of hollow nanotube cross-section and cross-section of $W_{18}O_{49}$@WSe_2 nanowhisker are displayed in the upper right corners of the figures (b) and (c), respectively.

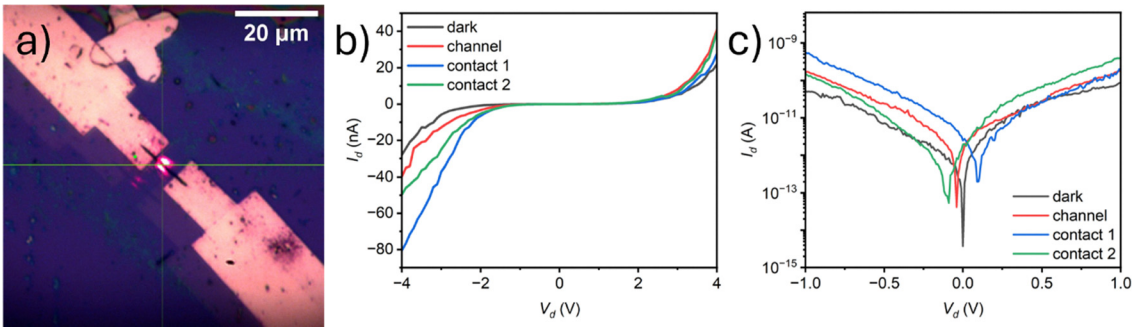

Fig. 5 (a) Optical image of the 2-contact device with the laser spot at the center of the nanotube (channel). Typical *I*–*V* curve of the WSe_2 nanotube device in linear (b) and $\log_{10}$ scale (c).

Low-temperature (−170 °C) SEM-cathodoluminescence (CL) measurement was performed on a hollow WSe_2 nanotube (Fig. 4b) and a $W_{18}O_{49}$@WSe_2 nanowhisker (Fig. 4c). The SEM images of the corresponding structures are displayed in Fig. S5. The hollow WSe_2 nanotubes exhibit two characteristic emission peaks corresponding to the A (697 nm) and B excitons (650 nm) of WSe_2.[14,36] In contrast, the core–shell $W_{18}O_{49}$@WSe_2 nanowhiskers show a different emission behavior: the spectrum is dominated by luminescence from the tungsten oxide core[37] (broad signal ranging from 350–550 nm) together with the B exciton emission (maximum at 650 nm) from the WSe_2 shell, while the A exciton emission is strongly quenched. This quenching likely originates from charge transfer or non-radiative recombination pathways at the oxide–WSe_2 interface, indicating strong electronic interaction between the oxide core and the WSe_2 shell. Importantly, a significant blueshift of the WSe_2 excitonic emissions is linked to lowering the sample's temperature[38] and strain.[36,39] It was shown before that WS_2 nanotubes with a mean diameter of 90 nm support cavity modes and a strong coupling effect, which was clearly revealed in optical scattering (extinction) experiments. In sharp contrast to that, the CL of a single tube of such nanotubes at −140 °C revealed pure excitonic emission.[40] Putatively, the electron beam is unable to produce coherent cavity modes in the core of the nanotubes, which may explain the absence of the strong coupling effect in the CL measurements.

Additionally, optical extinction measurements were performed at room temperature for the nanotubes dispersed in acetone solution (Fig. S6). The α and β peaks at 1.57 eV (790 nm), 2.016 eV (615 nm) are lower in energy than the literature values of the A exciton- 1.65–1.66 eV (750–745 nm) and B exciton 2.13 (582 nm).[41–43] The dips in the spectra (1.65 and 2.15 eV) closely agree with the excitons' energy. The inset table in Fig. S6 summarizes the positions of the extinction spectrum peaks. Using SEM images, the size (diameter) distribution of the nanotubes was analyzed. The mean value of the nanotubes' diameter (80 nm) suggests that the α peak in the extinction spectrum is the lowest polariton mode produced by strong coupling between optical cavity modes entrapped in the nanotube lumen and the A exciton.[10,14] The β peak in the extinction spectrum could possibly be associated with the upper A polariton and the lower B polariton, but the present methodology is unable to resolve the two peaks separately.

Electrical performance tests on the devices at room temperature showed that their current–voltage (*I*–*V*) curves indicate the semiconducting nature of the WSe_2 nanotubes and the formation of back-to-back Schottky barriers at the contact interfaces. The nanotube outline within the electrode region results from conformal top-contact deposition, and the cylindrical nanotube creates a local ridge on the evaporated metallic film. This topography induces non-specular scattering in optical microscopy, producing the observed contrast, as shown in Fig. 5a. The dark current of the device (Fig. 5a) was generally small, with values only on the order of tens of nA (±4 V) and tens of pA at a bias voltage of 1 V, as shown in Fig. 5b and c, respectively. Under 633 nm laser illumination, the device exhibited photoresponse characteristics. When the laser was irradiated on the device channel area and the electrode contact areas, the device showed a photoeffect (Fig. 5b). Particularly, when the laser was placed on the electrode contact area, the device exhibited a clear photovoltaic response, further confirming the presence of the localized Schottky barrier. The test results showed that its photovoltaic voltage was about 0.1 V. The photovoltaic current was on the order of pA, as shown in Fig. 5c. The measured photoeffect of these devices was much inferior compared to WS_2 nanotubes.[44] The relatively weak photovoltaic response could imply strong photothermal effects and promising photocatalytic activity, which might be advantageous for other applications. Additionally, $W_{18}O_{49}$@WSe_2 nanowhiskers were measured in a 2-point contact arrangement (Fig. S7a). Expectably, the metallic conductivity of the oxide core governed the *I*–*V* curve, *i.e.* linear shape akin to an Ohmic contact (Fig. S7b).

Conclusions

Almost mm-long WSe_2 nanotubes with an aspect ratio of up to 10^4 are reported in this work. These ultra-long nanotubes were synthesized by first reacting hydrogen tungsten oxide bronze in a sealed ampoule, followed by the conversion of the resulting ultra-long $W_{18}O_{49}$ nanowhiskers through reaction with a continuous flow of selenium vapor at elevated temperatures. A detailed characterization of the nanotubes was undertaken primarily using high-resolution TEM and related techniques. Hybrid 1D/2D WSe_2 nanotube/platelets and core–shell $W_{18}O_{49}$@WSe_2 1D

nanostructures were produced as well. Such hybrid morphologies may offer interesting (photo)catalytic applications. Optical extinction measurements of the nanotubes affirmed the strong-coupling effect and the formation of exciton polaritons. Single-nanotube devices were established for electrical transport measurements at room temperature. The nanotubes exhibited semiconducting behavior and small photoeffects. Further investigation is required to elucidate the optical and electrical properties of such nanotubes in greater detail. Future work will focus on improving the synthetic protocol and the electrical transport properties, as well as the photoresponse of the long WSe_2 nanotubes.

Experimental

Preparation of the WO_{3-X} precursor nanowhiskers

A dark blue powder, hydrogen tungsten bronze, H_XWO_3 (1 g, X = 0.23–0.33), was used for the preparation of the WO_{3-Y} precursor. The material was sealed under vacuum (10^{-5} Torr) in a quartz ampule (13 cm in length). The powder was evenly spread along the entire length of the ampule and placed in a horizontal furnace, where it was sintered at 900 °C for 180 min.

Synthesis of the WSe_2 nanotubes

The continuous layer of $W_{18}O_{49}$ nanowhiskers was placed on one side of a boat (20.5 cm long), and 7 quartz crucibles containing a copious amount of selenium powder were placed on the opposite side. The boat was put into a horizontal flow reactor at 850 °C with a forming gas (5% H_2 in N_2, 100 mL min^{-1}). Initially, it was held in the cooler zone and then periodically shifted toward the center of the reactor every 15 minutes. After the final shift, it was left in the reactor for an additional 15 minutes, bringing the reaction time to 2 h.

Electron microscopy

Thermo Fisher Versa 3D microscope (20 kV; 0.12 nA) was used for SEM analysis. TEM analysis was performed using a double aberration-corrected Themis-Z microscope (Thermo Fisher Scientific Electron Microscopy Solutions, Hillsboro, USA) at an accelerating voltage 200 kV. Some measurements were executed on a Thermo Fisher Scientific Talos F200i equipped with a SuperX EDS detector. Both transmission and scanning transmission modes used a high accelerating voltage of 200 kV and a beam current of 1 nA. TEM, STEM, High-angle annular dark-field (HAADF), and images of energy dispersive X-ray spectroscopy (EDS) chemical mapping were post-processed in the Velox and ImageJ software.

Focused ion beam (FIB)

The cross-sectional TEM-lamellae were prepared using FIB Helios 5 FX (Thermo Fisher Scientific). Nanotubes were selected based on their contrast at 30 kV at which the presence of a hollow core or oxide nanowire is apparent. Carbon deposition (both electron- and ion-beam-induced) was used as a protection layer. FIB milling was done at accelerating voltages between 30 and 2 kV. For the Raman scattering pristine samples were dispersed in an ethanol solution using an ultrasonic bath and then drop-cast onto a clean silicon (100) wafer substrate. All Raman measurements were performed with a Horiba LabRAM HR spectrometer, equipped with a built-in He/Ne laser tuned to a wavelength of 633 nm, a 100× objective lens, and an 1800 g mm^{-1} grating. Spectra were acquired with 20-second accumulations, 60 accumulation cycles, and a laser power of 5 mW, as measured at the sample position.

SEM-cathodoluminescence

SEM-CL data were acquired using a Monarc Pro CL detector (Gatan) integrated into a Helios G4 Plasma FIB system (Thermo Fisher Scientific). Samples were maintained at −170 °C using a Gatan liquid-nitrogen-cooled stage. Hyperspectral maps and panchromatic CL images were collected at an accelerating voltage of 5 keV and beam current of 1.6 nA. For hyperspectral datasets, a 300 L mm^{-1} grating with a 15 nm bandpass was used, and the detector was centered at either 550 nm or 750 nm.

Optical extinction measurements

Optical extinction measurements were performed using a Bruker Vertex 80v FTIR Spectrometer operated in transmission mode. The sample solution was placed in a 10 mm quartz cuvette, while another cuvette with an ethanol solution was measured as the background reference. A halogen lamp was employed as the near-infrared (NIR) light source, in combination with a CaF_2 beamsplitter and a silicon diode detector. The absorbance spectrum was obtained by dividing the sample spectrum by the background spectrum. Measurements were carried out with a spectral resolution of 2 cm^{-1} and a phase resolution of 2 cm^{-1}. A Mertz phase correction method, a Norton–Beer (medium) apodization function, and a zero-filling factor of 2 were used for data processing.

Electrical transport measurements

WSe_2 nanotubes were dispersed onto Si/SiO_2 (500 nm) wafer, and their positions were identified through optical microscopy. For device fabrication, the WSe_2 nanotubes were dispersed onto Si/SiO_2 (500 nm) substrates. Top-contact electrodes (20 nm Ti/80 nm Au) were fabricated *via* electron beam lithography, electron beam evaporation, and lift-off in acetone. The Ti layer forms the contacting interface with the WSe_2 nanotube, while the Au layer serves as the conducting capping layer. We further performed photoelectric performance measurements on the WSe_2 nanotube devices with a laser wavelength of 633 nm. The spot size was 1.5 μm, and the laser intensity was 0.40 mW.

Author contributions

VK – conceptualization, data curation, formal analysis, investigation, methodology, supervision, validation, visualization, writing – original draft, writing – review & editing; VH – investigation, methodology, visualization, validation; SK – investigation, visualization; RPB – investigation, data curation,

visualization, writing – original draft, writing – review & editing; DDVdG – investigation, data curation; SR – investigation, data curation, methodology; ZZ – investigation, data curation, methodology; KB – investigation, data curation, validation; LH – investigation, data curation; XG – investigation, data curation; YG – investigation, validation, methodology, writing – original draft, writing – review & editing, supervision; PA – investigation, validation, methodology, writing – original draft, writing – review & editing, supervision; RT – conceptualization, funding acquisition, methodology, project administration, supervision, resources, validation, writing – original draft, writing – review & editing.

Conflicts of interest

There are no conflicts of interest to declare.

Data availability

The data supporting this article have been included as part of the supplementary information (SI). Supplementary information is available. See DOI: https://doi.org/10.1039/d6tc01050d.

Further informations and dataset are available on request.

Acknowledgements

VK acknowledges financial support from the Masaryk University under the MASH StG/CoG project no. MUNI/SC/2047/2025. We acknowledge the Cryo-electron microscopy and tomography core facility CEITEC MU of CIISB, Instruct-CZ Centre, supported by MEYS CR (LM2023042) and European Regional Development Fund-Project, Innovation of Czech Infrastructure for Integrative Structural Biology (No. CZ.02.01.01/00/23_015/0008175). RT acknowledges the support of the Magnus Konow Foundation in honor of his mother Olga Konow Rappaport. We also acknowledge the Irving and Cherna Moskowitz Center for Nano and Bio-Nano Imaging of the Weizmann Institute. The Perlman Family Foundation and the Kimmel Center for Nanoscale Science are greatly acknowledged.

References

1 S. Manzeli, D. Ovchinnikov, D. Pasquier, O. V. Yazyev and A. Kis, *Nat. Rev. Mater.*, 2017, **2**, 17033.
2 R. Ganatra and Q. Zhang, *ACS Nano*, 2014, **8**, 4074–4099.
3 W. Choi, N. Choudhary, G. H. Han, J. Park, D. Akinwande and Y. H. Lee, *Mater. Today*, 2017, **20**, 116–130.
4 X. Hu, K. Liu, Y. Cai, S.-Q. Zang and T. Zhai, *Small Sci.*, 2022, **2**, 2200008.
5 I. Shaheen, I. Hussain, T. Zahra, M. S. Javed, S. S. A. Shah, K. Khan, M. B. Hanif, M. A. Assiri, Z. Said, W. U. Arifeen, B. Akkinepally and K. Zhang, *J. Energy Storage*, 2023, **72**, 108719.
6 S. Bandi and A. K. Srivastav, *J. Mater. Sci.*, 2021, **56**, 6615–6644.
7 L. Yadgarov and R. Tenne, *Small*, 2025, **21**, 2400503.
8 M. Serra, R. Arenal and R. Tenne, *Nanoscale*, 2019, **11**, 8073–8090.
9 L. Yadgarov, B. Višić, T. Abir, R. Tenne, A. Y. Polyakov, R. Levi, T. V. Dolgova, V. V. Zubyuk, A. A. Fedyanin, E. A. Goodilin, T. Ellenbogen, R. Tenne and D. Oron, *Phys. Chem. Chem. Phys.*, 2018, **20**, 20812–20820.
10 S. S. Sinha, A. Zak, R. Rosentsveig, I. Pinkas, R. Tenne and L. Yadgarov, *Small*, 2020, **16**, 2070022.
11 G. Seifert, H. Terrones, M. Terrones, G. Jungnickel and T. Frauenheim, *Phys. Rev. Lett.*, 2000, **85**, 146–149.
12 Md. A. Rahman, Y. Yomogida, A. Ahad, K. Ueji, M. Nagano, A. Ihara, H. Nishidome, M. Omoto, S. Saito, Y. Miyata, Y. Gao, S. Okada and K. Yanagi, *Sci. Rep.*, 2023, **13**, 16959.
13 N. Zibouche, M. Ghorbani-Asl, T. Heine and A. Kuc, *Inorganics*, 2014, **2**, 155–167.
14 M. B. Sreedhara, Y. Miroshnikov, K. Zheng, L. Houben, S. Hettler, R. Arenal, I. Pinkas, S. S. Sinha, I. E. Castelli and R. Tenne, *J. Am. Chem. Soc.*, 2022, **144**, 10530–10542.
15 D. S. Dovzhenko, S. V. Ryabchuk, Yu. P. Rakovich and I. R. Nabiev, *Nanoscale*, 2018, **10**, 3589–3605.
16 X. Liu, T. Galfsky, Z. Sun, F. Xia, E. Lin, Y.-H. Lee, S. Kéna-Cohen and V. M. Menon, *Nat. Photonics*, 2015, **9**, 30–34.
17 Q. Wang, L. Sun, B. Zhang, C. Chen, X. Shen and W. Lu, *Opt. Express*, 2016, **24**, 7151.
18 V. Kundrát, R. Rosentsveig, K. Bukvišová, D. Citterberg, M. Kolíbal, S. Keren, I. Pinkas, O. Yaffe, A. Zak and R. Tenne, *Nano Lett.*, 2023, **23**, 10259–10266.
19 X. Han, Z. Qi, V. Kundrat, H. Li, Z. Li, X. Guo, P. Mao, W. Zheng, S. Hou, R. Liu, H. Wu, P. Wang, A. Zak, W. Liu, R. Tenne and Y. Guo, *Nat. Commun.*, 2026, **17**, 1514.
20 H. Kim, S. J. Yun, J. C. Park, M. H. Park, J. Park, K. K. Kim and Y. H. Lee, *Small*, 2015, **11**, 2192–2199.
21 Y. Yomogida, Y. Kainuma, T. Endo, Y. Miyata and K. Yanagi, *Appl. Phys. Lett.*, 2020, **116**, 203106.
22 V. Kundrat, E. Parth, R. Pinna Brito, H. Shalom, P. Immanuel, J. Zalesak, L. Houben, A. Kossoy, L. Yadgarov, P. Ayala and R. Tenne, *Chem. Mater.*, 2025, **37**(15), 5966–5973.
23 Y. Q. Zhu, W. K. Hsu, H. Terrones, N. Grobert, B. H. Chang, M. Terrones, B. Q. Wei, H. W. Kroto, D. R. M. Walton, C. B. Boothroyd, I. Kinloch, G. Z. Chen, A. H. Windle and D. J. Fray, *J. Mater. Chem.*, 2000, **10**, 2570–2577.
24 K. Bukvisova, L. Novak and V. Kundrat, *Nano Lett.*, 2026, **26**(16), 5566–5571.
25 V. Kundrát, L. Novák, K. Bukvišová, J. Zálešák, E. Kolíbalová, R. Rosentsveig, M. B. Sreedhara, H. Shalom, L. Yadgarov, A. Zak, M. Kolíbal and R. Tenne, *ACS Nano*, 2024, **18**, 12284–12294.
26 A. Margolin, R. Rosentsveig, A. Albu-Yaron, R. Popovitz-Biro and R. Tenne, *J. Mater. Chem.*, 2004, **14**, 617.
27 P. Chithaiah, S. Ghosh, A. Idelevich, L. Rovinsky, T. Livneh and A. Zak, *ACS Nano*, 2020, **14**, 3004–3016.
28 M. Remskar, M. Virsek and A. Jesih, *Nano Lett.*, 2008, **8**, 76–80.
29 B. Kim, N. Park and J. Kim, *Nat. Commun.*, 2022, **13**, 3237.

30 F. Qin, W. Shi, T. Ideue, M. Yoshida, A. Zak, R. Tenne, T. Kikitsu, D. Inoue, D. Hashizume and Y. Iwasa, *Nat. Commun.*, 2017, **8**, 14465.
31 H. Sahin, S. Tongay, S. Horzum, W. Fan, J. Zhou, J. Li, J. Wu and F. M. Peeters, *Phys. Rev. B: Condens. Matter Mater. Phys.*, 2013, **87**, 165409.
32 Y. Ding, Y. Wang, J. Ni, L. Shi, S. Shi and W. Tang, *Phys. B*, 2011, **406**, 2254–2260.
33 Y. Pan and D. R. T. Zahn, *Nanomaterials*, 2022, **12**, 3949.
34 C. Blaga, Á. Labordet Álvarez, A. Balgarkashi, M. Banerjee, A. Fontcuberta, I. Morral and M. Dimitrievska, *Nanoscale Adv.*, 2024, **6**, 4591–4603.
35 E. Del Corro, H. Terrones, A. Elias, C. Fantini, S. Feng, M. A. Nguyen, T. E. Mallouk, M. Terrones and M. A. Pimenta, *ACS Nano*, 2014, **8**, 9629–9635.
36 S. B. Desai, G. Seol, J. S. Kang, H. Fang, C. Battaglia, R. Kapadia, J. W. Ager, J. Guo and A. Javey, *Nano Lett.*, 2014, **14**, 4592–4597.
37 K. Thummavichai, N. Wang, L. Cheong Lem, M. Phillips, C. Ton-That, H. Chang, C. Hu, F. Xu, Y. Xia and Y. Zhu, *Mater. Lett.*, 2018, **214**, 232–235.
38 S. M. Oliver, J. Young, S. Krylyuk, T. L. Reinecke, A. V. Davydov and P. M. Vora, *Commun. Phys.*, 2020, **3**, 10.
39 S. Ghosh, V. Brüser, I. Kaplan-Ashiri, R. Popovitz-Biro, S. Peglow, J. I. Martínez, J. A. Alonso and A. Zak, *Appl. Phys. Rev.*, 2020, **7**, 041401.
40 S. Ghosh, V. Brüser, I. Kaplan-Ashiri, R. Popovitz-Biro, S. Peglow, J. I. Martínez, J. A. Alonso and A. Zak, *Appl. Phys. Rev.*, 2020, **7**, 041401.
41 Q. Cui, F. Ceballos, N. Kumar and H. Zhao, *ACS Nano*, 2014, **8**, 2970–2976.
42 Z. Ahmadi Heidari and M. Knupfer, *Phys. Rev. B*, 2025, **111**, 205205.
43 A. Arora, M. Koperski, K. Nogajewski, J. Marcus, C. Faugeras and M. Potemski, *Nanoscale*, 2015, **7**, 10421–10429.
44 Y. J. Zhang, T. Ideue, M. Onga, F. Qin, R. Suzuki, A. Zak, R. Tenne, J. H. Smet and Y. Iwasa, *Nature*, 2019, **570**, 349–353.